



A meshless wave-based method for modeling sound propagation in three-dimensional axisymmetric lined ducts

Tengjiao He^{1,5} · Shiqi Mo² · Erzheng Fang² · Xinyu Liu³ · Yong Li⁴

Received: 29 June 2023 / Accepted: 15 September 2023

© The Author(s), under exclusive licence to Springer-Verlag London Ltd., part of Springer Nature 2023

Abstract

Theoretical modeling of sound propagation within lined ducts can help with interpreting the underlying mechanisms of waveguide physics. Herein, we present ESM-FLOW, a meshless, wave-based method in physical space for modeling sound propagation in 3D axisymmetric lined ducts. First, ESM-FLOW is applied to a 3D axisymmetric problem with uniform flow, in which the wall-reflected fields are replaced by a set of equivalent sources (ESs) surrounding the wall. A circumferential Fourier transform is employed to reduce this to a 2D problem in the circumferential modal domain. This enables efficient solving using a 2D equivalent-source method (ESM) scheme with circumferential modal Green's functions. Clenshaw–Curtis quadrature is used to accurately evaluate the oscillating circumferential integral. The unknown ES amplitudes are solved for through a linear system assembled by replacing the incident and wall-reflected fields with ESs satisfying the wall boundary conditions in the modal domain. Next, rigid-wall modes are derived as inputs for the 3D axisymmetric problem, enabling modal analysis—something with which most boundary-integral formulation (BIF) methods struggle. Finally, a multi-layer ESM-FLOW method is presented to address medium inhomogeneities, in which the non-uniform waveguide is divided into layers with piece-wise constant medium properties. ESM-FLOW is validated by comparison with a finite-element model, and additional simulations are presented to showcase its capabilities. The results demonstrate that ESM-FLOW combines the numerical efficiency and accuracy of typical BIF methods (including backscattering) while overcoming the limitations imposed by uniform media. This makes it highly applicable to the acoustic design of engines and ventilation systems.

Keywords Sound propagation · Lined duct · Waveguide · Boundary integral

1 Introduction

Being able to analyze sound propagation in non-uniform waveguides is very important in areas such as room acoustics, aeroacoustics, underwater acoustics, and the acoustic design and optimization of engines and ventilation systems [1, 2]. In particular, there is a need in these applications to maximize the acoustic attenuation associated with sound propagation through a flow duct by lining the duct walls [3–6]. Modeling sound propagation in lined ducts with flows helps to increase the understanding of the underlying mechanisms of waveguide physics and thus guides optimization of the attenuation performance of the liner at the preliminary design stage. Nevertheless, the corresponding modeling work is computationally challenging, as the model must account for both the propagation behaviors associated

with non-uniform waveguides and the effects of flows on sound waves.

Two types of approach can be used to model sound propagation in a lined flow duct: semi-analytical and fully numerical. Examples of the former are the segmentation approach [7, 8] and the multimodal method [9], also known as the coupled-mode method in underwater acoustics [10]. The segmentation approach uses a stepwise approximation to divide a non-uniform waveguide into several uniform segments so that the modal-coupling coefficients can be solved for by assembling all segments using the boundary conditions across the interfaces between pairs of adjacent segments. This method can shed light directly on the waveguide physics, and it is thus a powerful tool for analyzing the underlying propagation mechanisms. However, when dealing with high-frequency problems, large numbers of segments and modes are required to obtain convergent solutions, and this significantly increases the computational burden. Furthermore, the number of modes

Extended author information available on the last page of the article

involved in the computation must be considered carefully when mode coupling occurs. In contrast, the multimodal method relies on the concept of modal projection, in which eigenmodes are projected onto a space spanned by a group of local modes. The unknown modal coefficients are then solved for by propagating the traveling modes through an admittance condition. Unlike the segmentation approach, this method circumvents the stepwise approximation, thus achieving better convergence. Nevertheless, the convergence deteriorates severely when discontinuities arise in the boundaries with respect to the propagation range, and high-frequency problems will still impose a heavy computational burden.

Unlike semi-analytical methods, fully numerical methods (with appropriate numerical and discretization schemes) are unconditionally stable for treating arbitrary non-uniform waveguides, tending to converge toward the exact solution of the wave equation. Classic numerical methods include the finite-element method (FEM) [5, 11, 12] and the meshless wave (MW)-based approach. The FEM aims to solve the weak form of the wave equation, relying on volume discretization of the physical domain. One very attractive aspect of the FEM is its high versatility regarding the material properties treated in the simulation, which makes it suitable for handling non-uniform flows. Nevertheless, depending on the meshing size, the size of problems that can be handled by the FEM is restricted by the available computational power. This means that the FEM becomes cumbersome when performing parametric sweeps or Monte Carlo simulations in the acoustic design of engines and ventilation systems.

Recent years have seen a growing emphasis on MW-based approaches within the realm of computational engineering. For example, one approach involves the construction of node control domains [13], which are seamlessly integrated with the finite-volume method to address the challenges of porous flows featuring singular source terms. Recently, a spatially approximated MW-based method has been developed to tackle an extensive spectrum of time-fractional partial differential equations in both 2D and 3D domains [14] encompassing both regular and irregular geometries. By virtue of their meshless nature, MW-based techniques circumvent the time-consuming and troublesome pretreatment process, and they thus exhibit superior numerical efficiency when compared with the FEM. Illustratively, a representative MW-based technique, the boundary-integral formulation (BIF) [15, 16], has found widespread application in addressing complex boundary-value problems inherent to the field of acoustics. A pertinent illustration in this context involves the use of a local knot method, which can be effectively employed to address large-scale acoustic problems related to room acoustics, noise prediction in vehicles, and modeling of sound propagation in bi-material plates [17–19].

Due to the swift advancement of its affiliated algorithms, which are aimed at enhancing accuracy, efficiency, and stability, the boundary-element method (BEM) has garnered significant attention within the realm of acoustic engineering, particularly concerning the problem of sound propagation in the presence of fluid motion. The BEM reduces the size of a problem by discretizing only the boundaries treated in the simulation, thus solving the wave equation more efficiently than methods based on volume discretization. In scenarios involving sound propagation under uniform flow conditions, the BEM typically involves the Lorentz transformation [20], thereby allowing the convected Helmholtz equation to be reformed into the standard Helmholtz equation, for which a standard BEM scheme can be implemented. One issue associated with the Lorentz transformation is the deformation of physical space, which increases the complexity of the form of the boundary conditions and the numerical scheme for the coupled equations [21, 22]. Although this issue can be circumvented by implementing the BIF in the physical domain [15, 23–26], the BEM suffers inherently from singularities arising from Green's functions. In addition, modeling medium inhomogeneities using the BIF method has long been an open problem. The goal of the present work was to fill these gaps.

As an alternative to the BEM, the equivalent-source method (ESM) was initially developed by Koopmann et al. [27] to solve for acoustic radiation. The basic idea of the ESM is to replace the sound field with a set of equivalent sources (ESs), with their unknown amplitudes obtained by matching the boundary conditions in the problem. Since these ESs are often distributed on a surface that is offset from the practical boundary, the singularity problem of the BEM is avoided. Furthermore, compared to the BEM, numerical implementation of the ESM is much simpler, and its computational complexity is much lower; this is because its basis functions are nodes rather than elements. It should be noted that the ESM is a meshless, wave-based approach that combines the numerical efficiency and accuracy of typical BIF methods. This means that it offers a full-wave solution that includes backscattering. The capabilities of the ESM for computational acoustics have been demonstrated in multiple areas [28], from room acoustics [29] to underwater acoustics [30–34]. In aeroacoustics, the ESM is commonly used to solve for sound scattering and acoustical holography for moving sources [35–38]. However, to the best of our knowledge, in physical space, no ESM-based sound-propagation model has been developed to solve for sound propagation in a lined duct, especially for situations in which the medium within the duct is non-uniform.

The primary contributions of this paper are as follows: (i) a meshless method based on the ESM, namely ESM-FLOW, is developed to solve for sound propagation in a 3D axisymmetric lined duct, along with full formulations developed

in physical space; (ii) expressions for rigid-wall modes are derived as inputs for ESM-FLOW, and in particular, spinning modes are obtained, which may help with the imposition of nonaxisymmetric source conditions in future work; (iii) a multi-layer ESM-FLOW model is first developed to handle medium inhomogeneities within the duct, in which the non-uniform waveguide is divided into layers, each with piece-wise constant medium properties. Numerical simulations are presented to validate ESM-FLOW and to showcase its capabilities in modal analysis and acoustic optimization of liners. Its numerical stability and efficiency are also investigated in detail, including parameter selection and the optimized Clenshaw–Curtis quadrature scheme [39] for the circumferential integral. The key aspect of ESM-FLOW is that it is presented in the physical domain without approximations (except for numerical discretization approximations), and it thus converges to the exact wave-propagation solution.

The remainder of this paper is organized as follows: the formulation of ESM-FLOW is presented in Sect. 2, numerical simulations are presented in Sect. 3, and conclusions are drawn in Sect. 4.

2 Methods

This section introduces ESM-FLOW, an ESM-based sound-propagation model for a non-uniform lined duct. We present the frequency-domain formulations using the time convention $e^{i\omega t}$, where ω is the angular frequency, t is the time, and $i = \sqrt{-1}$. In the equations herein, we denote all matrices and vectors using upper- and lowercase bold letters, respectively.

2.1 Governing equation and boundary conditions

As shown in Fig. 1, we assume a 3D duct with a radius of η_a to be axisymmetric with respect to the x axis, along which a uniform mean flow moves with a positive velocity of v_0 . To represent the acoustic liner, the duct wall is characterized locally by an Ingard–Myers impedance boundary ($x_1 < x < x_2$), and by a Neumann boundary elsewhere. The homogeneous air within the duct has a density of ρ_0 and a sound speed of c_0 ; it is moving horizontally at a velocity of v_0 in the positive x direction. By assuming a harmonic time dependence for the velocity potential $\Phi(\mathbf{r}, \omega)$, the governing wave equation for steady-state linear acoustics in a uniform flow is given by [40]:

$$\nabla^2 \Phi(\mathbf{r}) + \frac{\omega^2}{c_0^2} \Phi(\mathbf{r}) - \frac{2i\omega v_0}{c_0^2} \frac{\partial \Phi(\mathbf{r})}{\partial x} - \frac{v_0^2}{c_0^2} \frac{\partial^2 \Phi(\mathbf{r})}{\partial x^2} = 0, \quad (1)$$

where $\mathbf{r} = (x, \eta \sin \theta, \eta \cos \theta)$ is a position vector, θ is the circumferential angle of a field point, and the acoustic pressure p is

$$p = -\rho_0 \left(i\omega + v_0 \frac{\partial}{\partial x} \right) \Phi. \quad (2)$$

The overall field satisfies the Ingard–Myers boundary condition [41] at the wall for field points at $\mathbf{r}_a = [x, \eta_a \sin \theta_a, \eta_a \cos \theta_a]$:

$$\frac{\partial \Phi}{\partial z} \Big|_{\mathbf{r}=\mathbf{r}_a} = \left(1 + \frac{v_0}{i\omega} \frac{\partial}{\partial x} \right) Y p \Big|_{\mathbf{r}=\mathbf{r}_a}, \quad (3)$$

where Y is the wall admittance.

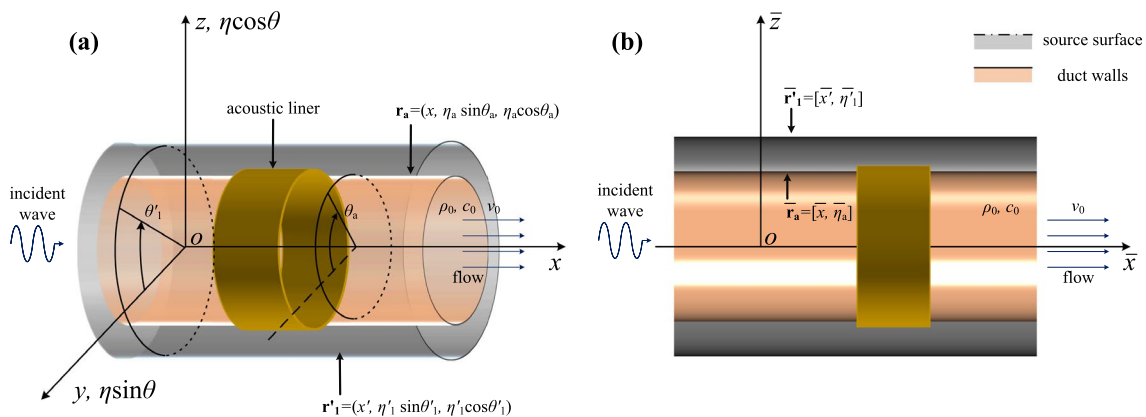


Fig. 1 Schematic of ESM-FLOW. The duct geometry is axisymmetric with respect to the x axis, along which a uniform mean flow is assumed. The shallow orange surface represents the duct walls, while

the surrounding outer grey surface denotes the surface upon which the ESs are distributed. The dark yellow surface is the acoustic liner that locally covers the duct

2.2 ESM-FLOW formulation for 3D axisymmetric sound propagation in a lined duct with uniform flow

ESM-FLOW expresses the solution of Eq. (1) as a linear combination of the basis functions $G_{\Phi}(\mathbf{r};\mathbf{r}'|K)$, also known as Green’s function. This means that the waveguide field is a superposition of fields generated by ESs. To simulate reflection by the wall, ESs are distributed on an axisymmetric surface surrounding the duct with a larger radius η'_1 , which is represented by the grey surface in Fig. 2a. The position vector of the ES surface is denoted by $\mathbf{r}'_1 = [x', \eta'_1 \sin \theta'_1, \eta'_1 \cos \theta'_1]$. Wall reflection can be expressed as

$$\Phi_r(\mathbf{r}_{(m)}) = \sum_{n=1}^N s(\mathbf{r}'_{1(n)})G_{\Phi}(\mathbf{r}_{(m)};\mathbf{r}'_{1(n)}|K), \tag{4}$$

where $s(\mathbf{r}'_1)$ represents the unknown ES amplitudes, the subscripts (n) and (m) denote the n th ES and m th point field, respectively, and N is the total number of ESs. The Green’s function $G_{\Phi}(\mathbf{r};\mathbf{r}'|K)$ is given by

$$G_{\Phi}(\mathbf{r};\mathbf{r}'|K) = \frac{e^{-iK[D-M(x-x')]}{4\pi D}, \tag{5}$$

where $K = k/\beta$ is the convected wavenumber, $k = \omega/c_0$ is the wavenumber, $\beta = \sqrt{1 - M^2}$ represents the flow dependence, $M = v_0/c_0$ is the Mach number, and $D = \sqrt{(x - x')^2 + \beta^2(\eta^2 + \eta'^2 - 2\eta\eta' \cos \varphi)}$. Here, $\varphi = \theta - \theta'$ is the circumferential angle between the meridian planes that include the field point at \mathbf{r} and the source point at \mathbf{r}' . Note that $G_{\Phi}(\mathbf{r};\mathbf{r}'|\omega)$ automatically satisfies the Sommerfeld radiation condition, making it suitable for constructing

the fundamental solution of the waveguide field as the basis functions without imposing any non-reflecting boundaries at each end of the waveguide. For a vector of field points $\mathbf{r}_{(1)}, \mathbf{r}_{(2)}, \dots, \mathbf{r}_{(N)}$, Eq. (4) can be written in matrix form as follows:

$$\Phi_r = \mathbf{G}_{\Phi}(\mathbf{r};\mathbf{r}'_1|K)\mathbf{s}. \tag{6}$$

Figure 2b depicts a 2D schematic of an axisymmetric duct in the meridian plane, in which $\bar{\mathbf{r}}_a = [\bar{x}, \bar{z}_a]$ and $\bar{\mathbf{r}}'_1 = [\bar{x}', \bar{z}'_1]$ denote the 2D coordinates of points at the wall and the ES surface, respectively and the overbars ($\bar{}$) indicate positions in the meridian plane.

The axisymmetric duct geometry ensures that the homogeneous medium flows in the axial direction, making the field quantities (i.e., velocity potential, pressure, and particle velocity) 2π -periodic functions of the circumferential angle. Thus, they can be expanded into a series of independent circumferential modes using a pair of circumferential Fourier transforms [42, 43]:

$$F_{3D}(\mathbf{r};\mathbf{r}') = \sum_{-\infty}^{+\infty} F_{\text{axis}}^j(\bar{\mathbf{r}};\bar{\mathbf{r}}') e^{ij\varphi}, \tag{7a}$$

$$F_{\text{axis}}^j(\bar{\mathbf{r}};\bar{\mathbf{r}}') = \frac{1}{2\pi} \int_0^{2\pi} F_{3D}(\mathbf{r};\mathbf{r}') e^{-ij\varphi} d\varphi, \tag{7b}$$

where $F_{3D}(\mathbf{r};\mathbf{r}')$ denotes the 3D field quantity at \mathbf{r} due to a source at \mathbf{r}' , and $F_{\text{axis}}^j(\bar{\mathbf{r}};\bar{\mathbf{r}}')$ denotes the Fourier coefficient of the j th mode.

Using these transforms, the problem’s dimensions reduce from 3D in the $(x, \eta \sin \theta, \eta \cos \theta)$ system to 2D in the meridian plane (\bar{x}, \bar{z}) . This avoids the need for repeated computations resulting from the periodic functions throughout the axisymmetric geometry and significantly reduces the numerical cost. Consequently, the 2D ESM-FLOW scheme can solve each circumferential modal equation in the meridian plane, with ESs distributed on a 1D line (as shown in Fig. 1b). For circumferential mode j , the total field resulting from reflection by the walls and the incident field satisfies the Ingard–Myers boundary condition [41] at the wall in the meridian plane for field points at $\bar{\mathbf{r}}_a$:

$$\left. \frac{\partial \Phi_t^j}{\partial z} \right|_{\mathbf{r}=\bar{\mathbf{r}}_a} = \left(1 + \frac{v_0}{i\omega} \frac{\partial}{\partial x} \right) \mathbf{Y} \mathbf{p}_t^j \Big|_{\mathbf{r}=\bar{\mathbf{r}}_a}, \tag{8}$$

where \mathbf{Y} is a diagonal admittance matrix with non-zero values at the diagonal positions corresponding to $x_1 < x < x_2$ and zeros elsewhere. The total velocity potential Φ_t^j and total acoustic pressure p_t^j for the circumferential mode j are given by

$$\Phi_t^j(\bar{\mathbf{r}}_a) = \Phi_{\text{inc}}^j(\bar{\mathbf{r}}_a) + \mathbf{G}_{\text{axis}-\Phi}^j(\bar{\mathbf{r}}_a;\bar{\mathbf{r}}'_1|K)\mathbf{s}_1^j, \tag{9a}$$

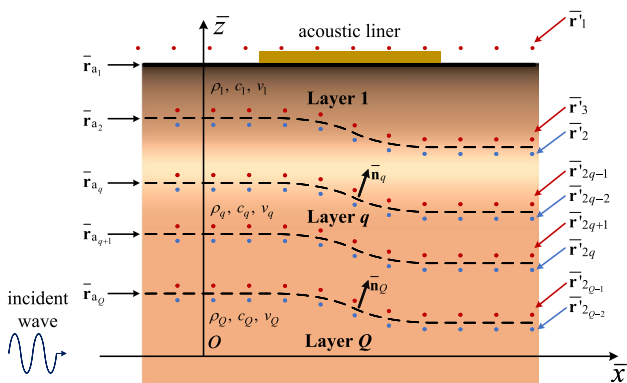


Fig. 2 Schematic of multi-layer ESM-FLOW method in the meridian plane in a waveguide of Q layers. The solid bold line and the dashed lines represent the actual duct wall and the interfaces between two adjacent layers of the waveguide, respectively. In the q th layer, each pair of red and blue dots at $\bar{\mathbf{r}}_{2q-1}$ and $\bar{\mathbf{r}}_{2q}$, respectively, represents those ESs producing the reflected fields from the adjacent upper layer (or the duct wall for $q = 1$) and lower layer, respectively

$$\mathbf{p}_t^j(\bar{\mathbf{r}}_a) = \mathbf{p}_{\text{inc}}^j(\bar{\mathbf{r}}_a) + \mathbf{G}_{\text{axis-}p}^j(\bar{\mathbf{r}}_a; \bar{\mathbf{r}}_1' | K) \mathbf{s}_1^j, \tag{9b}$$

where Φ_{inc}^j and $\mathbf{p}_{\text{inc}}^j$ are $N \times 1$ column vectors of the incident velocity potential and acoustic pressure, respectively, for mode j ; $\mathbf{G}_{\text{axis-}\Phi}^j$ and $\mathbf{G}_{\text{axis-}p}^j$ are $N \times N$ transfer matrices of the velocity potential and acoustic pressure, respectively, for mode j ; and \mathbf{s}_1^j is an $N \times 1$ column vector of ES amplitudes for mode j . According to Eq. (7), $\mathbf{G}_{\text{axis-}\Phi}^j$ is given by

$$\mathbf{G}_{\text{axis-}\Phi}^j(\bar{\mathbf{r}}_a; \bar{\mathbf{r}}_1' | K) = \frac{1}{2\pi} \int_0^{2\pi} \mathbf{G}_{\Phi}(\mathbf{r}_a; \mathbf{r}_1' | K) e^{-ij\varphi} d\varphi, \tag{10}$$

and $\mathbf{G}_{\text{axis-}p}^j$ can be obtained by first deriving the acoustic-pressure Green's functions based on Eq. (2) and then calculating the modal Green's functions using the Fourier transform given by Eq. (7)

$$\begin{aligned} \mathbf{G}_{\text{axis-}p}^j(\bar{\mathbf{r}}_a; \bar{\mathbf{r}}_1' | K) \\ = -\frac{1}{2\pi} \int_0^{2\pi} \rho_0 \left[i\omega + \nu_0 \frac{\partial}{\partial x} \right] \mathbf{G}_{\Phi}(\mathbf{r}_a; \mathbf{r}_1' | K) e^{-ij\varphi} d\varphi. \end{aligned} \tag{11}$$

We use Clenshaw–Curtis quadrature to evaluate the circumferential integral, which fits the oscillating nature of the integral kernel. This provides accurate and efficient results with only a few angular samplings, unlike the fast Fourier transform that is commonly used for evaluating the circumferential integral [44, 45]. Note that for the symmetric (zeroth) circumferential mode, the circumferential integral can be reduced to $\int_0^\pi \bullet \cos(-j\varphi) d\varphi$, which further improves the computation efficiency because it avoids repeated sampling from π to 2π .

After obtaining the modal Green's functions, we can rewrite the boundary conditions for mode j in terms of the ES amplitudes. Substituting Eq. (9) back into Eq. (8) gives

$$\begin{aligned} \text{LHS} &= \frac{\partial}{\partial z} \left[\Phi_{\text{inc}}^j(\bar{\mathbf{r}}_a) + \mathbf{G}_{\text{axis-}\Phi}^j(\bar{\mathbf{r}}_a; \bar{\mathbf{r}}_1' | K) \mathbf{s}_1^j \right], \\ \text{RHS} &= \mathbf{Y} \left[\mathbf{p}_{\text{inc}}^j(\bar{\mathbf{r}}_a) + \mathbf{G}_{\text{axis-}p}^j(\bar{\mathbf{r}}_a; \bar{\mathbf{r}}_1' | K) \mathbf{s}_1^j \right] \\ &\quad + \frac{\nu_0}{i\omega} \mathbf{Y} \frac{\partial}{\partial x} \left[\mathbf{p}_{\text{inc}}^j(\bar{\mathbf{r}}_a) + \mathbf{G}_{\text{axis-}p}^j(\bar{\mathbf{r}}_a; \bar{\mathbf{r}}_1' | K) \mathbf{s}_1^j \right] \\ &\quad + \frac{\nu_0}{i\omega} \mathbf{Y}' \left[\mathbf{p}_{\text{inc}}^j(\bar{\mathbf{r}}_a) + \mathbf{G}_{\text{axis-}p}^j(\bar{\mathbf{r}}_a; \bar{\mathbf{r}}_1' | K) \mathbf{s}_1^j \right]. \end{aligned} \tag{12}$$

Equalizing the left- and right-hand sides (LHS and RHS) of Eq. (8), and after some rearrangements of Eq. (12), this yields

$$\begin{aligned} \mathbf{G}_{\text{axis-}\Phi_z}^j(\bar{\mathbf{r}}_a; \bar{\mathbf{r}}_1' | K) \mathbf{s}_1^j + \mathbf{d}^j \\ = \mathbf{Y} \left[\Gamma^j \mathbf{s}_1^j + \mathbf{e}^j \right] \\ + \frac{\nu_0}{i\omega} \mathbf{Y}' \left[\mathbf{G}_{\text{axis-}p}^j(\bar{\mathbf{r}}_a; \bar{\mathbf{r}}_1' | K) \mathbf{s}_1^j + \mathbf{p}_{\text{inc}}^j(\bar{\mathbf{r}}_a) \right], \end{aligned} \tag{13}$$

where \mathbf{Y}' is the admittance derivative with respect to x , and

$$\Gamma^j = \left[1 + \frac{\nu_0}{i\omega} \frac{\partial}{\partial x} \right] \mathbf{G}_{\text{axis-}p}^j(\bar{\mathbf{r}}_a; \bar{\mathbf{r}}_1' | K), \tag{14a}$$

$$\mathbf{d}^j = \Phi_{\text{inc}_z}^j(\bar{\mathbf{r}}_a), \tag{14b}$$

$$\mathbf{e}^j = \left[1 + \frac{\nu_0}{i\omega} \frac{\partial}{\partial x} \right] \mathbf{p}_{\text{inc}}^j(\bar{\mathbf{r}}_a), \tag{14c}$$

in which the matrix $\mathbf{G}_{\text{axis-}\Phi_z}^j$ is given by

$$\mathbf{G}_{\text{axis-}\Phi_z}^j(\bar{\mathbf{r}}_a; \bar{\mathbf{r}}_1' | K) = \frac{1}{2\pi} \int_0^{2\pi} \frac{\partial}{\partial z} \mathbf{G}_{\Phi}(\mathbf{r}_a; \mathbf{r}_1' | K) e^{-ij\varphi} d\varphi, \tag{15}$$

and

$$\Phi_{\text{inc}_z}^j(\bar{\mathbf{r}}_a) = \frac{1}{2\pi} \int_0^{2\pi} \frac{\partial}{\partial z} \Phi_{\text{inc}}(\mathbf{r}_a) e^{-ij\varphi} d\varphi. \tag{16}$$

In Eq. (14), the horizontal derivatives of $\mathbf{p}_{\text{inc}}^j(\bar{\mathbf{r}}_a)$ and $\mathbf{G}_{\text{axis-}p}^j(\bar{\mathbf{r}}_a; \bar{\mathbf{r}}_1' | K)$ can be calculated by

$$\frac{\partial \mathbf{p}_{\text{inc}}^j(\bar{\mathbf{r}}_a)}{\partial x} = -\rho_0 \left(i\omega \frac{\partial}{\partial x} + \nu_0 \frac{\partial^2}{\partial x^2} \right) \Phi_{\text{inc}}, \tag{17a}$$

$$\begin{aligned} \frac{\partial \mathbf{G}_{\text{axis-}p}^j(\bar{\mathbf{r}}_a; \bar{\mathbf{r}}_1' | K)}{\partial x} &= -\frac{1}{2\pi} \int_0^{2\pi} \rho_0 \\ &\quad \left[i\omega \frac{\partial}{\partial x} + \nu_0 \frac{\partial^2}{\partial x^2} \right] \mathbf{G}_{\Phi}(\mathbf{r}_a; \mathbf{r}_1' | K) e^{-ij\varphi} d\varphi. \end{aligned} \tag{17b}$$

Finally, \mathbf{s}_1^j can be obtained by solving the inversion of Eq. (13):

$$\begin{aligned} \mathbf{s}_1^j &= \left[\mathbf{G}_{\text{axis-}\Phi_z}^j(\bar{\mathbf{r}}_a; \bar{\mathbf{r}}_1' | K) - \mathbf{Y}\Gamma^j - \frac{\nu_0}{i\omega} \mathbf{Y}' \mathbf{G}_{\text{axis-}p}^j(\bar{\mathbf{r}}_a; \bar{\mathbf{r}}_1' | K) \right]^{-1} \\ &\quad \left[-\mathbf{d}^j + \mathbf{Y}\mathbf{e}^j + \frac{\nu_0}{i\omega} \mathbf{Y}' \mathbf{p}_{\text{inc}}^j(\bar{\mathbf{r}}_a) \right]. \end{aligned} \tag{18}$$

2.3 Point-source and modal excitations

In this section, we derive the point-source and modal excitations for ESM-FLOW. The incident field due to a point source is considered first. We consider only the on-axial point-source case in the 3D axisymmetric situation. The off-axial source case can also be accounted for by a superposition of different circumferential modes, but this will not be given here to save space. In such a scenario, the incident velocity-potential Green's function due to the point source for circumferential mode j can be calculated by:

$$\Phi_{\text{inc}}^j(\bar{\mathbf{r}}_a) = 4\pi \times \frac{1}{2\pi} \int_0^{2\pi} G_\Phi(\mathbf{r}_a; \mathbf{r}'_1 | K) e^{-ij\varphi} d\varphi, \quad (19)$$

where $\bar{\mathbf{r}}'_s = (\bar{x}_s, 0)$ indicates the 2D plane coordinate of the on-axis point source. Since the on-axis point source is considered here, the Green's function $G_\Phi(\mathbf{r}_a; \mathbf{r}'_1 | K)$ is axisymmetric with respect to the x axis. As a result, the integral kernel, $G_\Phi(\mathbf{r}_a; \mathbf{r}'_1 | K)$, is independent of the circumferential mode, meaning that the integral in Eq. (19) can be calculated analytically. This yields

$$\Phi_{\text{inc}}^j(\bar{\mathbf{r}}_a) = 4\pi\xi G_\Phi(\bar{\mathbf{r}}_a; \bar{\mathbf{r}}'_s | K), \quad (20)$$

where $\xi = -\frac{1}{2\pi}$ for $j = 0$ and $\xi = -\frac{1}{i2\pi j}(e^{i2\pi j} - 1)$ otherwise.

Next, we give the expression of the rigid-wall mode excitation for the 3D axisymmetric ESM-FLOW method. In the 3D axisymmetric situation, the eigenmode of the rigid-wall mode is $J_j(\gamma_l^j \bar{z})$, and this gives

$$\Phi_{\text{inc}}^j(\bar{\mathbf{r}}_a) = \xi J_j(\gamma_l^j \bar{z}_a) e^{-i(\zeta_l^j - KM)(\bar{x}_a - \bar{x}_s)}, \quad (21a)$$

$$\Phi_{\text{inc}_z}^j(\bar{\mathbf{r}}_a) = \frac{\zeta_l^j}{2} \xi \left[J_{j+1}(\gamma_l^j \bar{z}_a) - J_{j-1}(\gamma_l^j \bar{z}_a) \right] e^{-i(\zeta_l^j - KM)(\bar{x}_a - \bar{x}_s)}, \quad (21b)$$

$$P_{\text{inc}}^j(\bar{\mathbf{r}}_a) = \xi \left[\omega - \nu_0(\zeta_l^j - KM) \right] J_j(\gamma_l^j \bar{z}_a) e^{-i(\zeta_l^j - KM)(\bar{x}_a - \bar{x}_s)}, \quad (21c)$$

where $J_j(\gamma)$ is a Bessel function of the j th kind, and γ_l^j is the l th root of $\frac{dJ_j(\gamma)}{d\gamma}$.

2.4 Multi-layer ESM-FLOW method for a non-uniform lined duct

So far, we have assumed that the background mean flow within the lined duct is uniform. However, the properties of a medium are generally inhomogeneous, and the sound propagation may be affected by these medium inhomogeneities. Here, we describe the effects of non-uniform flow on wave propagation by dividing the medium into layers in which the medium inhomogeneities are piece-wise constant.

As shown in Fig. 2, we consider a waveguide of Q layers. We define that the actual duct wall is placed at $\bar{\mathbf{r}}_{a_1}$, and the interface between the q th layer and the $q + 1$ th layer is located at $\bar{\mathbf{r}}_{a_q}$ ($q > 1$). Based on the concept of sound-field separation and the ESM-FLOW method, the waveguide field in the q th layer can be separated into the fields reflected by the adjacent upper layer (or the duct wall for $q = 1$) and

lower layer. These reflections from the layers are then replaced by a superposition of the fields produced by two sets of ESs, one above the upper boundary at $\bar{\mathbf{r}}_{2q-1}$ and the other below the lower boundary at $\bar{\mathbf{r}}_{2q}$, respectively. The Myers boundary condition at the duct wall and the continuities of pressure and normal displacement across each interface between all the pairs of adjacent layers are given by

$$\begin{cases} \frac{\partial \Phi_t^j}{\partial z} \Big|_{\mathbf{r}=\bar{\mathbf{r}}_{a_1}} = \left(1 + \frac{\nu_1}{i\omega} \frac{\partial}{\partial x}\right) \mathbf{Y} \mathbf{P}_t^j \Big|_{\mathbf{r}=\bar{\mathbf{r}}_{a_1}}, & q = 1, \\ \frac{\partial \Phi_t^j}{\partial \bar{n}_q} \Big|_{\mathbf{r}=\bar{\mathbf{r}}_{a_q}}^- = \frac{\partial \Phi_t^j}{\partial \bar{n}_q} \Big|_{\mathbf{r}=\bar{\mathbf{r}}_{a_q}}^+, & q > 1, \\ \mathbf{P}_t^j \Big|_{\mathbf{r}=\bar{\mathbf{r}}_{a_q}}^- = \mathbf{P}_t^j \Big|_{\mathbf{r}=\bar{\mathbf{r}}_{a_q}}^+, & q > 1, \end{cases} \quad (22)$$

where $\frac{\partial}{\partial \bar{n}_q} = \frac{\partial}{\partial \bar{n}_q(\bar{\mathbf{r}}_{a_q})} - \frac{\partial}{\partial x} M^2 \bar{n}_{q_x}$ is the normal-derivative operator that accounts for the impact of flow [26, 46], and $\bar{n}_q(\bar{\mathbf{r}}_{a_q}) = (\bar{n}_{q_x}, \bar{n}_{q_z})$ represents the normal vector of the interface at $\bar{\mathbf{r}}_{a_q}$. After substituting for the pressure and displacement in the boundary conditions given by Eq. (21) in terms of the ES amplitudes, this yields a linear system coupling all fields generated by $2Q - 1$ sets of ESs:

$$[\mathbf{G}^j] \{\mathbf{s}^j\}^T = \{\mathbf{w}\}^T, \quad (23)$$

where $\{\mathbf{s}^j\}^T$ is the unknown amplitude vector, which is given by

$$\{\mathbf{s}^j\}^T = \{\mathbf{s}_1^j, \mathbf{s}_2^j, \mathbf{s}_3^j, \mathbf{s}_4^j, \dots, \mathbf{s}_{2q-3}^j, \mathbf{s}_{2q-2}^j, \mathbf{s}_{2q-1}^j, \mathbf{s}_{2q}^j, \dots, \mathbf{s}_{2Q-3}^j, \mathbf{s}_{2Q-2}^j, \mathbf{s}_{2Q-1}^j\}^T, \quad (24)$$

and the right-hand-side vector $\{\mathbf{w}\}^T$ is the incident field quantity, which is composed of

$$\{\mathbf{w}\}^T = \{\mathbf{w}_1, \mathbf{w}_2, \mathbf{w}_3, \dots, \mathbf{w}_{2q-2}, \mathbf{w}_{2q-1}, \dots, \mathbf{w}_{2Q-2}, \mathbf{w}_{2Q-1}\}^T. \quad (25)$$

In the above linear system, the global coefficient matrix $[\mathbf{G}^j]$ can be written as

$$\mathbf{G}^j \in \mathbb{C}^{Q \times (2Q-1)} : [\mathbf{A}_1; \mathbf{A}_2; \dots; \mathbf{A}_q; \dots; \mathbf{A}_{Q-1}; \mathbf{A}_Q], \quad (26)$$

where

$$\mathbf{A}_1 \in \mathbb{C}^{1 \times (2Q-1)}, q = 1 : \begin{bmatrix} \Lambda_{1,1}^j & \Lambda_{1,2}^j & \dots \\ & & \underbrace{\dots}_{(2Q-3) \times \mathbf{O}} \end{bmatrix} \quad (27a)$$

$$\mathbf{A}_q \in \mathbb{C}^{2 \times (2Q-1)}, 1 < q < Q :$$

$$\begin{bmatrix} \dots & \Lambda_{q,2q-3}^j & \Lambda_{q,2q-2}^j & -\Lambda_{q,2q-1}^j & -\Lambda_{q,2q}^j & \dots \\ \underbrace{\dots}_{2(q-2) \times \mathbf{O}} & \mathbf{P}_{q,2q-3}^j & \mathbf{P}_{q,2q-2}^j & -\mathbf{P}_{q,2q-1}^j & -\mathbf{P}_{q,2q}^j & \underbrace{\dots}_{(2Q-2q-1) \times \mathbf{O}} \\ \vdots & \mathbf{P}_{q,2q-3}^j & \mathbf{P}_{q,2q-2}^j & -\mathbf{P}_{q,2q-1}^j & -\mathbf{P}_{q,2q}^j & \vdots \end{bmatrix} \quad (27b)$$

$$\mathbf{A}_Q \in \mathbb{C}^{2 \times (2Q-1)}, q = Q : \quad (27c)$$

$$\begin{bmatrix} \underbrace{\dots}_{(2Q-4) \times \mathbf{O}} & \Lambda^j_{Q,2Q-3} & \Lambda^j_{Q,2Q-2} & -\Lambda^j_{Q,2Q-1} \\ \vdots & \mathbf{P}^j_{Q,2Q-3} & \mathbf{P}^j_{Q,2Q-2} & -\mathbf{P}^j_{Q,2Q-1} \end{bmatrix}$$

where \mathbf{O} denotes an $N \times N$ zero matrix, and the matrix blocks $\Lambda^j_{q,h}$ and $\mathbf{P}^j_{q,h}$ are given by

$$\Lambda^j_{q,h} = \begin{cases} \mathbf{G}^j_{\text{axis-}\Phi_z}(\bar{\mathbf{r}}_{a_1}; \bar{\mathbf{r}}'_h | K_1) - \left[\mathbf{Y} + \frac{v_1}{i\omega} \mathbf{Y} \frac{\partial}{\partial x} + \frac{v_1}{i\omega} \mathbf{Y}' \right] \mathbf{G}^j_{\text{axis-}p}(\bar{\mathbf{r}}_{a_1}; \bar{\mathbf{r}}'_h | K_1), & (q = 1), \\ \frac{\partial}{\partial \bar{n}_q(\bar{\mathbf{r}}_{a_q})} \mathbf{G}^j_{\text{axis-}\Phi}(\bar{\mathbf{r}}_{a_q}; \bar{\mathbf{r}}'_h | K_{q-1}), & (q > 1, h = 2q - 3, 2q - 2), \\ \frac{\partial}{\partial \bar{n}_q(\bar{\mathbf{r}}_{a_q})} \mathbf{G}^j_{\text{axis-}\Phi}(\bar{\mathbf{r}}_{a_q}; \bar{\mathbf{r}}'_h | K_q), & (q > 1, h = 2q - 1, 2q), \end{cases} \quad (28a)$$

$$\mathbf{P}^j_{q,h} = \begin{cases} -\rho_{q-1} \left[1 + \frac{v_{q-1}}{i\omega} \frac{\partial}{\partial x} \right] \mathbf{G}^j_{\text{axis-}\Phi}(\bar{\mathbf{r}}_{a_q}; \bar{\mathbf{r}}'_h | K_{q-1}), & (q > 1, h = 2q - 3, 2q - 2), \\ -\rho_q \left[1 + \frac{v_q}{i\omega} \frac{\partial}{\partial x} \right] \mathbf{G}^j_{\text{axis-}\Phi}(\bar{\mathbf{r}}_{a_q}; \bar{\mathbf{r}}'_h | K_q), & (q > 1, h = 2q - 1, 2q), \end{cases} \quad (28b)$$

where the subscript q, h for each matrix block specifies the boundary field at $\bar{\mathbf{r}}_{a_q}$ produced by the ES placed at $\bar{\mathbf{r}}'_h$; and ρ_q, v_q , and K_q are the density, flow velocity, and convected wave-number of the q th layer, respectively. The RHS vector $\{\mathbf{w}\}^T$ is determined by providing an incident field. When the excitation by an on-axial point source in the Q th layer is considered, this incident field only interacts with the boundary at $\bar{\mathbf{r}}_Q$. This gives a sparse vector of $\{\mathbf{w}\}^T$ in which only the last two elements are calculated:

$$\{\mathbf{w}\}^T = \left\{ 0, \dots, 0, \frac{\partial}{\partial \bar{n}_Q(\bar{\mathbf{r}}_{a_Q})} \Phi^j_{\text{inc}}(\bar{\mathbf{r}}_{a_Q}), \mathbf{P}^j_{\text{inc}}(\bar{\mathbf{r}}_{a_Q}) \right\}^T. \quad (29)$$

When excitation by an individual mode is considered, we assume a plane source extending from the upper to the lower duct wall. This means that the source excitation exists in every layer. The incident field consequently interacts with each interface dividing the waveguide, and $\{\mathbf{w}\}^T$ becomes a full vector. This gives

$$\{\mathbf{w}\}^T = \left\{ -\Phi^j_{\text{inc}_z}(\bar{\mathbf{r}}_{a_1}) + \left[\mathbf{Y} + \frac{v_1}{i\omega} \mathbf{Y} \frac{\partial}{\partial x} + \frac{v_1}{i\omega} \mathbf{Y}' \right] \mathbf{P}^j_{\text{inc}}(\bar{\mathbf{r}}_{a_1}), -\frac{\partial}{\partial \bar{n}_2(\bar{\mathbf{r}}_{a_2})} \Phi^j_{\text{inc}}(\bar{\mathbf{r}}_{a_2}), \dots, \frac{\partial}{\partial \bar{n}_Q(\bar{\mathbf{r}}_{a_Q})} \Phi^j_{\text{inc}}(\bar{\mathbf{r}}_{a_Q}), \mathbf{P}^j_{\text{inc}}(\bar{\mathbf{r}}_{a_Q}) \right\}^T. \quad (30)$$

To enhance the stability of the inversion process that is employed to solve the linear system in Eq. (23)—particularly given the relatively sparse nature of the coefficient matrix—a matrix-scaling technique is employed. This technique involves permutation and rescaling of the matrix $[\mathbf{G}^j]$.

The objective of this technique is to formulate a new coefficient matrix

$$\mathbf{H} = \mathbf{SR}[\mathbf{G}^j]\mathbf{F}, \quad (31)$$

which is characterized by diagonal elements of magnitude 1 and off-diagonal entries bounded by a magnitude of 1. This strategic modification yields an enhancement in the condition of the coefficient matrix. This is achieved by reformulating Eq. (23) as

$$\mathbf{H}\mathbf{y} = \mathbf{b}, \quad (32)$$

where

$$\{\mathbf{s}^j\}^T = \mathbf{F}\mathbf{y}, \quad (33a)$$

$$\mathbf{b} = \mathbf{SR}\{\mathbf{w}\}^T. \quad (33b)$$

In this context, \mathbf{S} signifies the permutation-information matrix, which is characterized by entries of magnitude 1, while \mathbf{S} and \mathbf{F} correspond to the row and column scaling matrices, respectively. These matrices can be effectively generated through using the `equilibrate` function in MATLAB. A comprehensive delineation of the algorithmic procedure is available in Ref. [47]. After permuting and rescaling $[\mathbf{G}^j]$, the resultant sparse linear system, which is characterized by an improved condition number, is amenable to solution through either lower-upper (LU) matrix factorization or the generalized minimal residual (GMRE) method. It should be noted that the convergence of the iteration solver involved in the GMRE method can be significantly improved by preconditioning the system with the incomplete LU factorization of \mathbf{H} . Given that an exhaustive exploration of the linear system solver lies beyond the scope of this article, we present only a formulation of the general process associated with solving Eq. (32) through the LU matrix factorization.

The LU algorithm facilitates the factorization of a row-permuted rendition (\mathbf{H}_{rp}) of the square input matrix \mathbf{H} in the form

$$\mathbf{H}_{\text{rp}} = \mathbf{L}\mathbf{U}, \quad (34)$$

wherein \mathbf{L} symbolizes a lower triangular square matrix characterized by unity diagonal elements, while \mathbf{U} denotes an upper triangular square matrix. The matrix factors are substituted for \mathbf{H}_{rp} in

$$\mathbf{H}_{\text{rp}}\mathbf{y} = \mathbf{b}_{\text{rp}}, \quad (35)$$

where \mathbf{b}_{rp} is the row-permuted variant of \mathbf{b} . The resulting equation

$$\mathbf{L}\mathbf{U}\mathbf{y} = \mathbf{b}_{\text{rp}} \quad (36)$$

is solved for by substituting $\mathbf{g} = \mathbf{U}\mathbf{y}$ and solving two triangular systems:

$$\mathbf{Lg} = \mathbf{b}_{rp}, \tag{37a}$$

$$\mathbf{Uy} = \mathbf{g}. \tag{37b}$$

After solving the unknown ES amplitudes, the waveguide field in each layer can be reconstructed by summing up reflections replaced by the two sets of ESs above and below the layer interfaces.

3 Numerical simulations

In this section, we present the results of various numerical simulations. First, to benchmark ESM-FLOW, it is validated in comparison with FEM models for problems associated with sound propagation in a lined duct with uniform flow. Next, to demonstrate ESM-FLOW’s capability for modal analysis, the fields excited by rigid-wall modes in the flow duct are calculated. After that, multi-layer ESM-FLOW model is used to simulate sound propagation in a lined duct with non-uniform flow.

To implement ESM-FLOW, one set of ESs is placed at the conformal line above the duct wall in the meridional plane. These are offset from the corresponding walls by the same stand-off distance. The ESs are distributed at the conformal lines with element length Δ between two adjacent ESs of $\hat{\lambda}/8$ and a stand-off distance d_s of 4Δ , where $\hat{\lambda} = (c_0 - |v_0|/f)$ is the convected wavelength. See Sect. 3.1.1 for a detailed

discussion of the ES configuration. The circumferential integral is evaluated using Clenshaw–Curtis quadrature with 72 samplings. The parameters are set to their default values unless otherwise specified. The simulations were implemented in MATLAB on a computer with an Intel Core i9-10900K CPU and 96 GB of RAM.

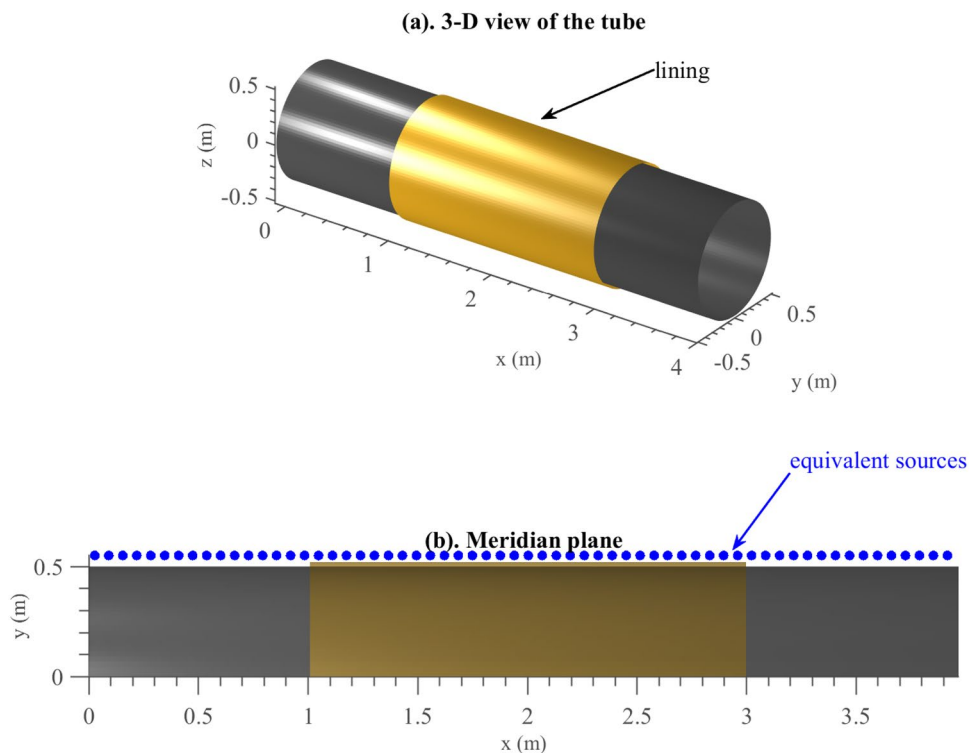
3.1 Sound propagation in a lined duct with uniform flow

In this section, we discuss sound propagation in a 3D axisymmetric lined flow duct, as shown in Fig. 3. The duct is axisymmetric around the x axis, with a radius of 0.5 m and a length of 4.0 m. The duct wall is partially lined between $x_1 = 1$ m and $x_2 = 3$ m, with the impedance coefficient determined by

$$Y(x) = \begin{cases} Y_1 \sin^2 \left[\frac{\pi(x - x_1)}{2\epsilon} \right], & x_1 < x \leq x_1 + \epsilon, \\ Y_1, & x_1 + \epsilon < x < x_2 - \epsilon, \\ Y_1 \sin^2 \left[\frac{\pi(x_2 - \epsilon - x)}{2\epsilon} \right], & x \geq x_2 - \epsilon, \end{cases} \tag{38}$$

where $\epsilon = 0.3$, and Y_1 is consistent with that in the validation case, which is $(0.192 + 0.096i)$ Pa·s/m. The density ρ and sound speed c of the air are 1 kg/m^3 and 340 m/s , respectively.

Fig. 3 Schematic of 3D axisymmetric tube treated in simulations, with the subplots showing (a) a perspective view and (b) an end view in the meridional plane. The liner is represented by the yellow surface surrounding the tube. The ESs in the meridional plane are marked by the blue dots offset from the tube wall

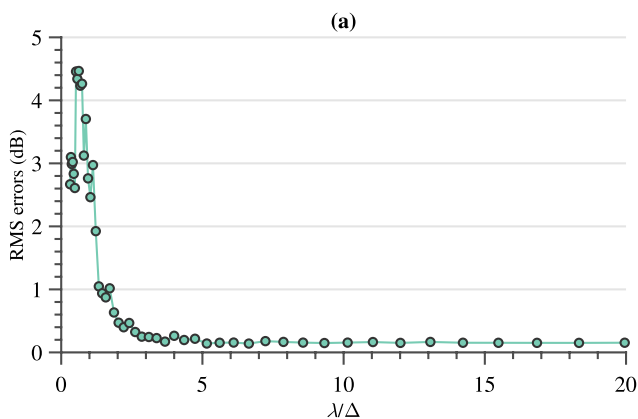


3.1.1 ES configuration

Before performing further numerical simulations using ESM-FLOW, we must determine the ES configuration required for convergent results. As many previous authors have shown, a conformal ES configuration is more numerically stable and more accurate than other configurations [30–32], and so a conformal ES configuration is used herein. The other main factors to determine are the element length Δ between adjacent ESs and the stand-off distance d_s from the corresponding boundary. First, the root-mean-square error is given by

$$E = \frac{1}{N} \sum_{n=1}^N \left| 10 \log \left\{ \left| \frac{p}{p_{\text{ref}}} \right| \right\} \right|, \quad (39)$$

where p_{ref} and p are the sound pressures calculated by the FEM and ESM-FLOW, respectively, along the line at $z = 0$ m with N sampling points. In this case, the sound pressure field was calculated by setting plane-wave incidence (zeroth mode) for $M = -0.7$ at $f = 1000$ Hz. In Fig. 4a, E is plotted as a function of the ratio of the convected wavelength $\hat{\lambda}$ to Δ with $d_s = 4\Delta$. As can be seen, E is large when Δ is greater than $\hat{\lambda}/2$ but decreases rapidly otherwise. This behavior is equivalent to the Nyquist criterion for sampling waveforms, suggesting that the ES distribution requires at least two points per $\hat{\lambda}$. To guarantee convergent solutions, we suggest $\Delta = \hat{\lambda}/8$. Next, E is plotted in Fig. 4b as a function of the ratio of d_s to $\hat{\lambda}$ with $\Delta = \hat{\lambda}/8$. The error decreases significantly with increasing d_s , remaining lower than 1 dB when $d_s > \Delta$ but eventually rebounding as d_s exceeds 10Δ . The large errors for small d_s are induced by the singularities of the Green’s functions, and those associated with large d_s are caused by instability in the inverse problem for large matrix conditions. Based on this, we recommend a stand-off distance of $d_s = 4\Delta$.



3.1.2 Parameter selection for evaluation of the circumferential integral

Next, we determine the parameters for evaluation of the circumferential integral. To demonstrate the high numerical efficiency and accuracy achieved with Clenshaw–Curtis quadrature, we compare its results with those obtained using the standard approach to deal with the circumferential integral. The standard integration scheme uses the Fourier transform of the circumferential expansion, performing the integration with the circumferential mode $e^{-ij\varphi}$ from zero to 2π with uniform samplings. The comparison is made for sound propagation with plane-wave incidence at 1000 Hz for a Mach number of -0.7 , and all other parameters remain at their default values. Figure 5a shows the sound pressure level (SPL) along a line at $z = 0$ m with the circumferential integral evaluated using Clenshaw–Curtis quadrature and the standard approach. The result obtained using the standard approach diverges significantly from the reference FEM solution with 72 samplings, but it improves gradually with increasing samplings. However, Clenshaw–Curtis quadrature with only 72 samplings shows smaller errors than those obtained with the standard approach using eight times as many samplings, thereby demonstrating the former’s high numerical efficiency and accuracy.

The reasons that Clenshaw–Curtis quadrature is suitable for dealing with the circumferential integral are that (i) the integral is highly oscillatory and (ii) the kernel of the circumferential integral oscillates rapidly as the integration variable approaches zero and 2π but tends to be much smoother otherwise. The latter is the reason that the uniform sampling scheme in the standard approach is inaccurate: it may provide insufficient samplings in the region in which the kernel oscillates rapidly, thus decreasing the accuracy of

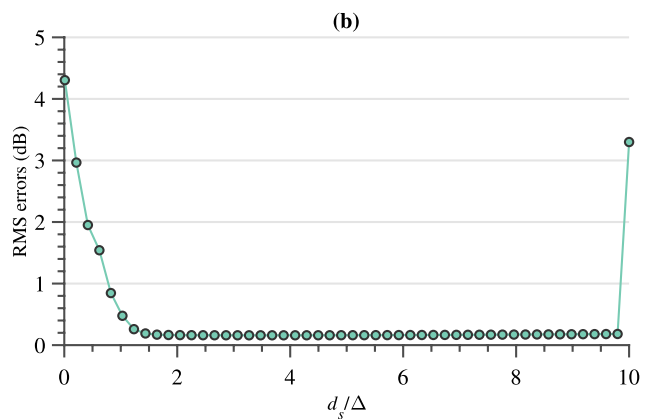


Fig. 4 Root-mean-square error as a function of (a) the ratio of the convected wavelength $\hat{\lambda}$ to the element length Δ between adjacent ESs along the conformal surface and (b) the ratio of the stand-off distance

d_s to $\hat{\lambda}$, calculated using the pressure along the line at $z = 0$ m. Here, $d_s = 4\Delta$ for (a) and $\Delta = \hat{\lambda}/8$ for (b)

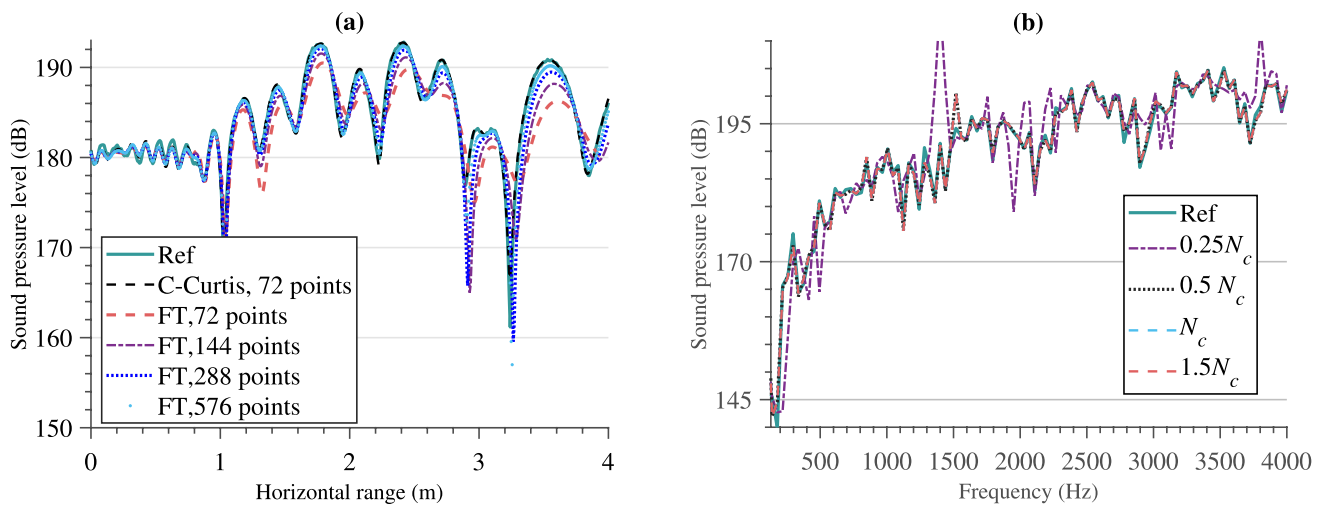


Fig. 5 (a) SPLs along a line at $z = 0$ m at 1000 Hz for a Mach number of -0.7 , with the circumferential integral evaluated using Clenshaw–Curtis quadrature and the standard approach. (b) SPLs at the

field point $(3.5, 0, 0)$ m over a frequency range of 100–4000 Hz for a Mach number of -0.7 , calculated using Clenshaw–Curtis quadrature with different circumferential samplings

the evaluation of the oscillating integral. In contrast, Clenshaw–Curtis quadrature provides uneven sampling across the integration range, with denser samplings at the upper and lower limits of the integration range [39], which fits the nature of the kernel oscillations exactly.

A key parameter to determine in Clenshaw–Curtis quadrature is the number of samplings for the circumferential integral. Here, this is determined via numerical simulations. In this case, the Mach number remains at -0.7 , along with the same plane-wave incidence input. The number of uniform circumferential samplings is defined as $N_c = 2\pi\eta/\lambda$, where η is the radius of the ES surface. Figure 5b shows the SPLs calculated using different numbers of circumferential samplings at the field point $(3.5, 0, 0)$ m over a frequency range of 100–4000 Hz, suggesting that the number of circumferential samplings should be larger than $0.5N_c$. Considering the compromise between numerical stability across a wide frequency range and computational efficiency, we suggest that the number of circumferential samplings should be N_c , and this is used as the default value herein. It is worth mentioning that the frequency sweep performed took about 30 min using FEM, but it took no more than 10 min using ESM-FLOW with $1.5N_c$. This confirms the high numerical efficiency of ESM-FLOW.

3.1.3 Model validation

Next, we validate ESM-FLOW by comparison with the FEM in the case of propagation from a monopole point source. The duct geometry and impedance-boundary setup remain the same as those in Sect. 3.1.1, but we now consider a monopole point source of unit mass flow rate [an amplitude of $1 \text{ kg}/(\text{m}\cdot\text{s})$] placed at $(0.5, 0, 0)$ m. The left-hand column

of Fig. 6 shows the SPL calculated by the FEM and ESM-FLOW with a receiver height of 1.5 m at different frequencies for $M = -0.7$ (with the reference pressure being $20 \mu \text{ Pa}$). Excellent agreement with the FEM results can be seen at each frequency, thus demonstrating the high degree of numerical accuracy that ESM-FLOW provides. The sound fields shown in the right-hand column of Fig. 6 exhibit apparent interference patterns. The higher the frequency, the stronger the interference; this is because higher modes resulting in stronger interference are cut-on at higher source frequencies.

3.1.4 Modal analysis

ESM-FLOW is a tool that allows for the analysis of the propagation of individual modes by introducing a plane-wave input with height-dependent amplitudes. Herein, modal analysis is employed to investigate the underlying propagation behavior within the flow duct. The simulation parameters used are the default settings. Figure 7 illustrates the propagation of the first three spinning modes (left-hand column) and axial modes (right-hand column) in the flow duct.

The fundamental features of the axial modes are the pronounced focusing effects along the $z = 0$ axis. Prior to reaching the lined region, their oscillation patterns in the standing-wave structures (eigenmodes) are defined by their eigenvalues. Each axial eigenmode oscillates from vertical to oblique as it traverses the lined region while simultaneously undergoing amplitude attenuation close to the lined wall and resonance along the $z = 0$ axis. The detailed depiction of the sound field near $x = 1$ m in Fig. 7 indicates a sudden change in the mode shape from cosine to sine when the sound wave passes through the cross sections

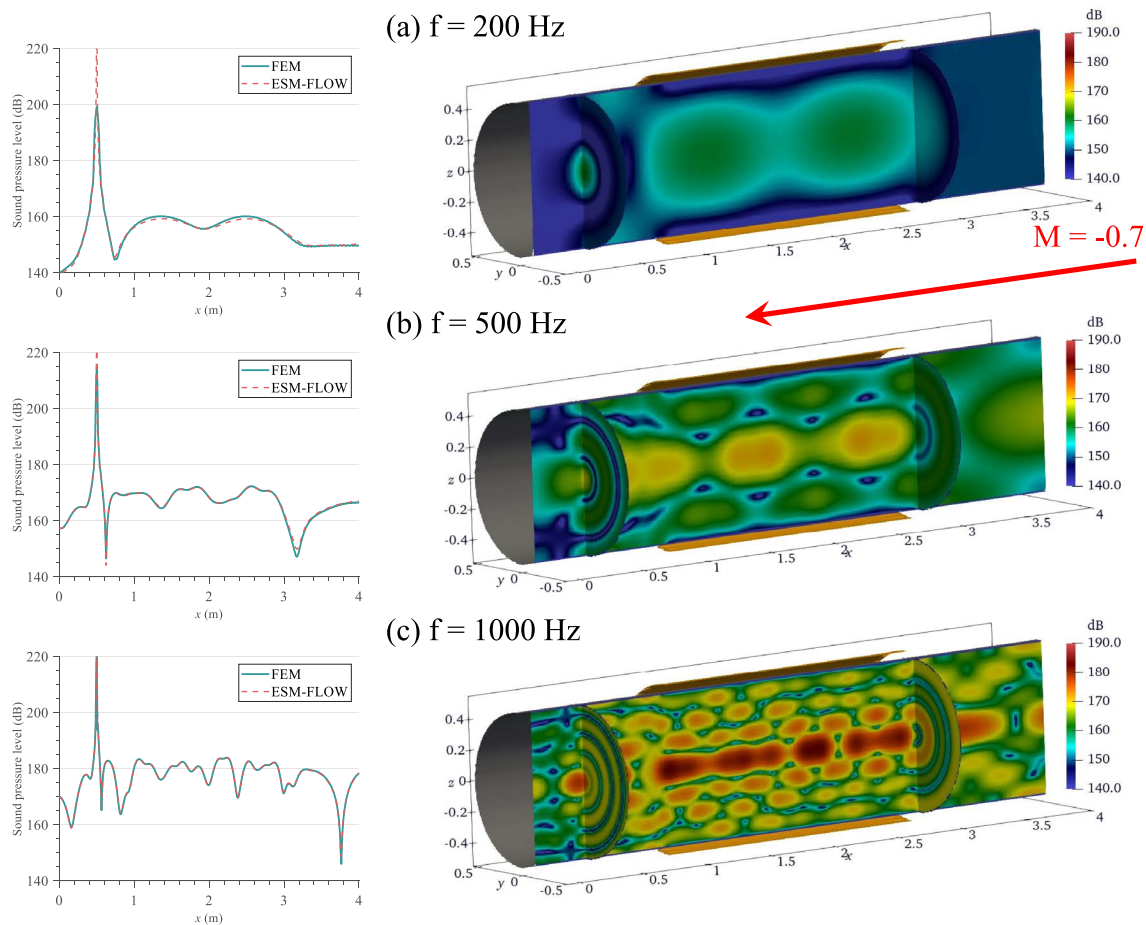


Fig. 6 SPLs in flow duct as calculated by the FEM and ESM-FLOW, with a receiver height of 0 m, at (a) 200 Hz, (b) 500 Hz, and (c) 1000 Hz for $M = -0.7$ (left-hand column). The green solid and red dashed lines denote the results from FEM and ESM-FLOW, respectively.

The right-hand column shows the corresponding sound fields at these frequencies, with the yellow surface surrounding the duct wall representing the liner

with and without a liner. This behavior can be attributed to the fact that the source mode derived in ESM-FLOW corresponds to the rigid-wall mode. In the presence of a lined duct wall, the mode becomes a linear combination of the rigid-wall modes. For example, the lowest lined-wall mode is constructed by linearly combining the two rigid-wall modes. Additionally, because only two modes are supported in the waveguide, the (0,2) mode is cut off and exhibits evanescent characteristics along the x axis.

In contrast to the axial modes, the spinning modes demonstrate destructive patterns along the $z = 0$ axis and tend to propagate along the duct wall. As the modal coupling induced by the liner occurs solely within either the spinning or axial modes, the spinning modes tend to maintain a standing-wave structure within the lined region. The aforementioned analysis demonstrates the versatility of ESM-FLOW in examining the underlying mechanisms

governing how a lining influences the propagation of individual modes in a flow duct.

3.2 Sound propagation in a 3D axisymmetric non-uniform lined duct with non-uniform flow

Finally, we proceed to calculate the sound propagation in a 3D axisymmetric lined duct with non-uniform flow. The 3D axisymmetric lined duct remains unchanged throughout the analysis. In this particular scenario, we will consider an unrealistic three-layer non-uniform flow, as depicted in Fig. 8. The lower boundaries of the first two outer layers are determined by the following expressions: $0.5 - 0.15e^{-(x-2)^2} - 0.05$ and $0.5 - 0.3e^{-(x-2)^2} - 0.1$, respectively. These expressions define the shape of the lower boundaries as functions of the axial coordinate x . From the outer to inner layers, the Mach number

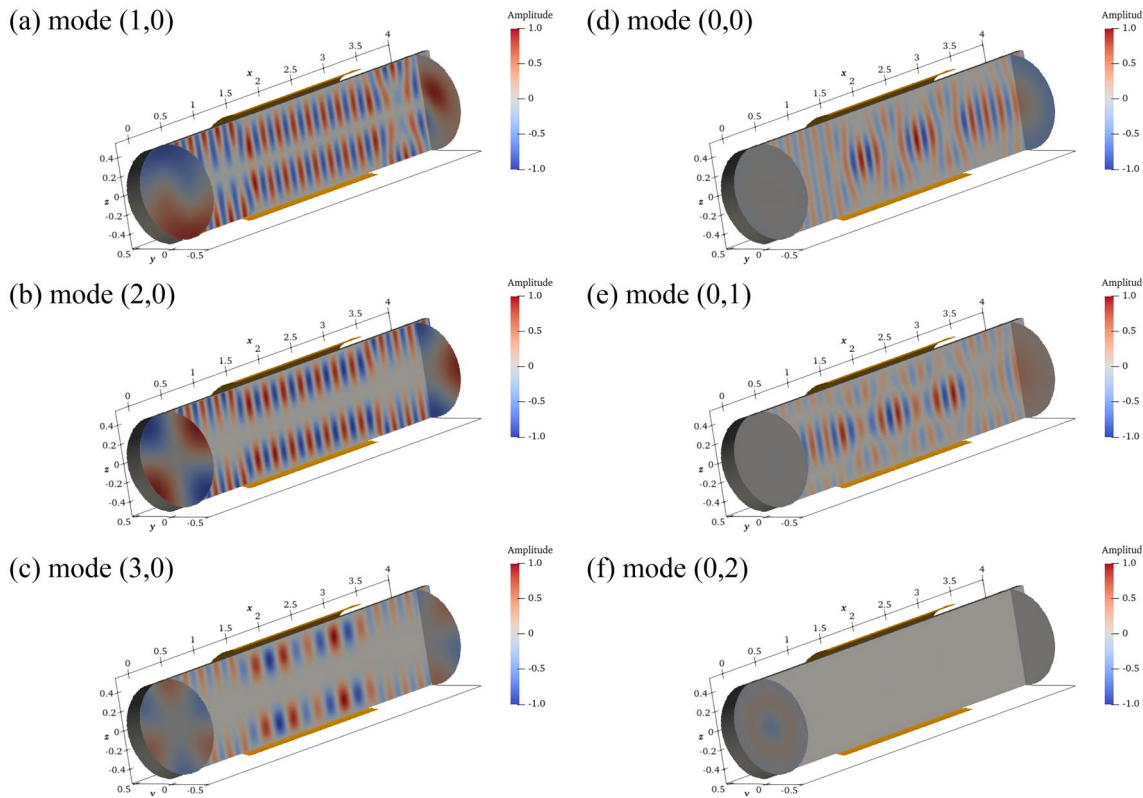


Fig. 7 Propagation (real part of sound pressure) of individual modes in 3D flow duct for $M = -0.7$ at 500 Hz. The duct wall is characterized by a localized Myer impedance boundary ($1 < x < 3$) and Neu-

mann boundaries elsewhere, with the yellow surface surrounding the duct wall representing the liner. The left- and right-hand columns display the spinning and axial modes, respectively

linearly increases from -0.5 to -0.7 , along with a linearly decreased air density from 1.05 to 0.95 kg/m^3 . Excitation by an on-axial point source with a frequency of 500 Hz is considered. This source emits sound waves that will propagate through the non-uniform flow inside the duct, undergoing modifications due to its changing acoustic properties.

To demonstrate the impact of non-uniform flow on sound propagation, we initially present the results obtained without the acoustic liner. As shown in Fig. 9, the results obtained from the multi-layer ESM-FLOW approach show remarkable agreement with the FEM results displayed in the first row. These findings validate the effectiveness of the multi-layer ESM-FLOW approach, with only minor deviations observed toward the end of the waveguide.

These deviations could be attributed to truncation errors, which have a minimal impact on the overall accuracy. Here, we also compare the condition numbers of the original coefficient matrix $[G^j]$ and that of the rescaled matrix \mathbf{H} , showcasing the effectiveness of the matrix scaling used in this work, which enhances the system's condition. The condition numbers of $[G^j]$ and \mathbf{H} are 1.66×10^{10} and 1.11×10^8 , respectively. This demonstrates that the matrix condition can be significantly improved using the matrix-scaling technique described at the end of Sect. 2.4.

For the purpose of comparison, Fig. 9c also illustrates the results obtained by ESM-FLOW in the presence of uniform flow with a Mach number of -0.7 . In this uniform scenario, a distinctive mode-like pattern emerges, indicating the excitation of two axial modes. However, when non-uniform

Fig. 8 Setup of the duct with non-uniform flow

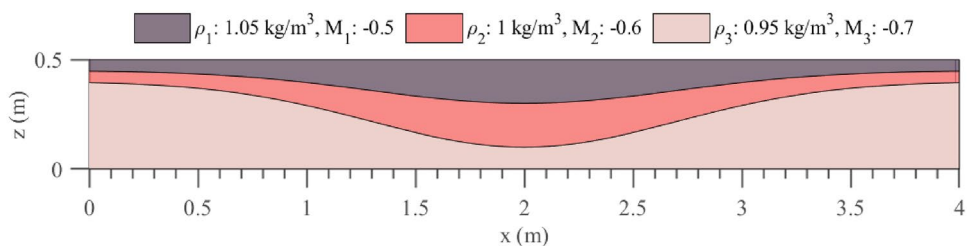


Fig. 9 Sound propagation in a rigid duct with non-uniform flow calculated by the FEM (top row) and ESM-FLOW (middle row), respectively, with an on-axial 500-Hz point source located at $x = 0.5$ m. For comparison purposes, the result obtained by ESM-FLOW in the presence of a uniform flow with a Mach number of -0.7 is shown in the bottom row. The results are given by SPL (in dB).

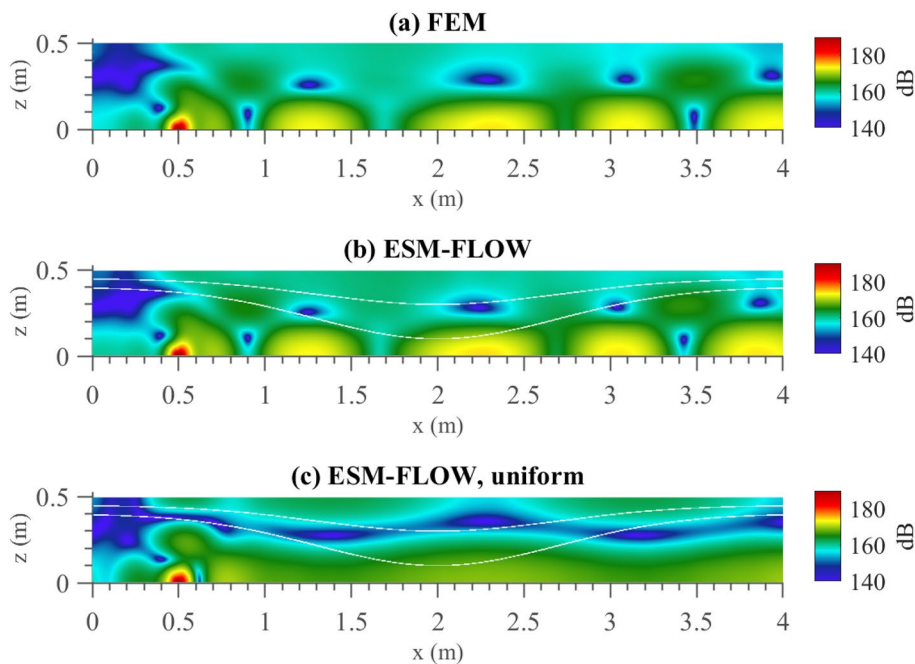
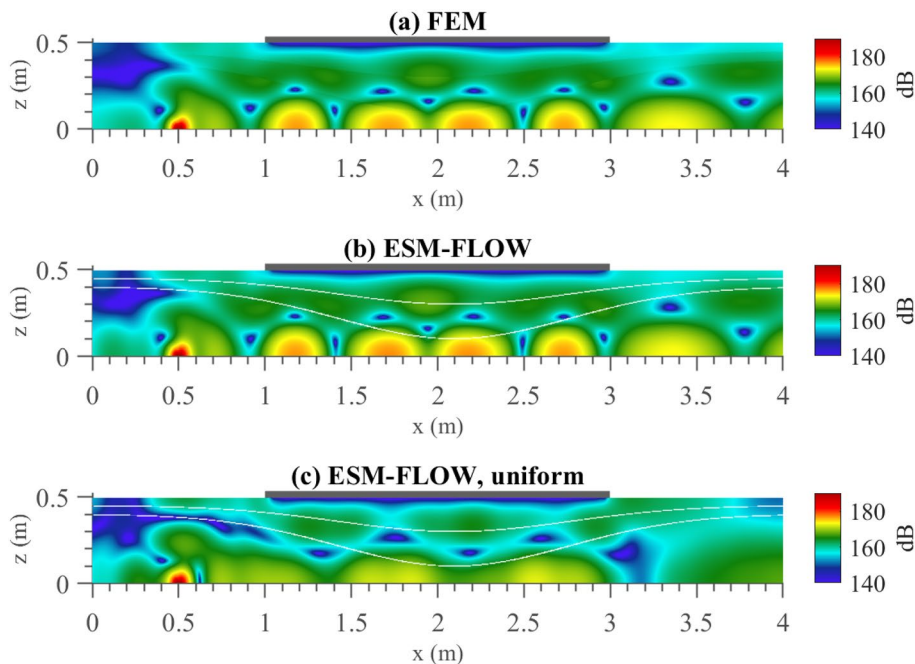


Fig. 10 Sound propagation in a lined duct with non-uniform flow calculated by the FEM (top row) and ESM-FLOW (middle row), respectively, with an on-axial 500-Hz point source located at $x = 0.5$ m. For comparison purposes, the result obtained by ESM-FLOW in the presence of a uniform flow with a Mach number of -0.7 is shown in the bottom row. The results are given by SPL (in dB).



flow is introduced, modal coupling occurs, causing energy to transition from low- to high-order axial modes. As a result, the non-uniform case exhibits the pattern associated with the third axial mode. Notably, more pronounced resonances along the x axis can be observed in the non-uniform flow case compared to the uniform flow scenario. This further emphasizes the influence of non-uniform flow on the sound-propagation characteristics.

Next, we present the results obtained after lining the duct wall. The lined region remains unchanged, and the same parameter values applied in the previous simulations are used for the acoustic liner. In Fig. 10, a comparison is made between the results obtained from the multi-layer ESM-FLOW approach and the FEM. Once again, both sets of results exhibit almost identical field patterns, thus confirming the accuracy and reliability of the multi-layer ESM-FLOW method. By further comparing Figs. 9 and

10, it becomes evident that the introduction of the acoustic liner enhances the localized resonance behavior observed along the x axis. Similarly, the uniform flow scenario exhibits weaker localized resonance behavior, indicating the influence of non-uniform flow on the modal-coupling phenomenon.

Overall, the inclusion of the acoustic liner in the analysis provides further insights into the impact of non-uniform flow on sound propagation, highlighting the significance of localized resonance effects. The close agreement between the multi-layer ESM-FLOW and FEM results emphasizes the accuracy and effectiveness of the multi-layer ESM-FLOW method in capturing these phenomena.

3.3 Numerical efficiency

In this section, we discuss the numerical efficiency of ESM-FLOW in comparison to the FEM for the same computational problem. The most computationally intensive step in ESM-FLOW is the solver used to obtain the ES amplitudes, as this involves solving a linear system. Consequently, the numerical efficiency of ESM-FLOW directly depends on the matrix size of the linear system, which corresponds to the number of unknowns to be solved.

For the FEM analysis, we employed the commercial software package COMSOL Multiphysics, using its linearized potential-flow model in the aeroacoustics module to account for the influence of flow on the sound field. The computation domain was discretized using a triangular mesh with a maximum element size set to one-eighth of the convected acoustic wavelength, ensuring compatibility with ESM-FLOW's discretization scheme. To ensure convergence, the computation domain was truncated using perfectly matched layers consisting of a mapping mesh comprising 40 layers with a total thickness of 0.5 m.

The numerical cost of the FEM is dependent on the number of degrees of freedom (N_{DOF}), which corresponds to the number of expansion coefficients to be solved. However, this number is expected to be much larger than the number of unknowns (N_{UN}) in ESM-FLOW for the same problem. This disparity arises because the FEM relies on volume discretization, whereas ESM-FLOW only discretizes the

boundaries of the problem. Generally, the numerical cost of the FEM scales as $O(N_{\text{DOF}}^2)$, while the numerical cost of ESM-FLOW scales as $O(N_{\text{UN}}^2 \times N_{\text{cm}})$, where N_{cm} denotes the number of circumferential modes.

Table 1 presents the computation times for the FEM and ESM-FLOW for the uniform flow problem simulated in Sect. 3, along with the numerical costs determined by N_{DOF} for the FEM and by N_{UN} for ESM-FLOW. As expected, the numerical cost of the FEM is between four and six orders of magnitude greater than that of ESM-FLOW, with a more significant difference observed at higher frequencies. This stark contrast demonstrates that ESM-FLOW is more suitable than the FEM for parametric-sweep studies, where efficiency is crucial. The efficiency advantage of ESM-FLOW becomes evident in Sect 3.1.2, where ESM-FLOW completed the frequency sweep in one-third of the computational time compared to FEM.

Furthermore, Table 2 compares the numerical costs for the uniform and non-uniform flow cases, indicating that increasing the number of layers only slightly increases the numerical cost. This analysis underlines the remarkable numerical efficiency provided by ESM-FLOW when compared to volume-discretization-based approaches.

It is essential to highlight that the comparisons made using the FEM serve the purpose of demonstrating that ESM-FLOW not only exhibits impressive numerical efficiency but also excels in accurately solving sound propagation under the influence of both uniform and non-uniform flows. Another rationale for employing the FEM as a benchmark arises from its provision of an explicit solution that attains convergence with the exact wave solution. Moreover, the absence of a comparable meshless method specifically tailored to addressing sound propagation within lined ducts necessitates the use of the FEM for comparison. Nevertheless, it is imperative to acknowledge that the FEM out-classes the proposed method in versatility, particularly when addressing intricate challenges like sound propagation amid the influence of shear flow. When it comes to the simplified engineering scenarios examined within this article, the proposed method has the advantage in terms of providing a good compromise between numerical efficiency and accuracy.

Table 1 Average computation times of the FEM and ESM-FLOW in the uniform flow computation cases

Frequency	200 Hz	500 Hz	1000 Hz
FEM [t]	1.0 s	1.5 s	2.5 s
ESM-FLOW [t]	0.08 s	0.18 s	0.53 s
FEM [O]	$O(10^7)$	$O(10^9)$	$O(10^{10})$
ESM-FLOW [O]	$O(10^5)$	$O(10^6)$	$O(10^6)$

Table 2 Average computation times of the FEM and ESM-FLOW in different 3D computation cases

Frequency	Uniform case 500 Hz	Non-uniform case 500 Hz
FEM(t)	1.5 s	1.5 s
ESM-FLOW(t)	0.18 s	0.7 s
FEM(O)	$O(10^9)$	$O(10^9)$
ESM-FLOW(O)	$O(10^6)$	$O(10^7)$

4 Conclusions

We have developed ESM-FLOW, a meshless, wave-based sound-propagation model for 3D axisymmetric lined ducts with flow. This model enables an efficient numerical solution of the convected Helmholtz equation. ESM-FLOW represents the wave solution by combining the fields generated by ESs (basis function superposition), which are distributed along a conformal line adjacent to the duct walls. The unknown amplitudes of these ESs are determined by solving a linear system, which is constructed by matching the wall boundary conditions (specifically, the Myer impedance-boundary condition).

To simplify the convected Helmholtz equation from 3D to 2D, we first apply a circumferential Fourier transform. The transform is numerically integrated using the Clenshaw–Curtis quadrature method. This reduction in dimensionality allows us to solve the 2D convected Helmholtz equation in the circumferential modal domain using a 2D version of ESM-FLOW. The Clenshaw–Curtis quadrature method is advantageous in terms of numerical efficiency, as it requires fewer circumferential samples compared to a uniform sampling scheme when dealing with the oscillating circumferential integral. Additionally, we derive expressions for rigid-wall modes, which serve as inputs for ESM-FLOW. This enables modal analysis, providing insights into the underlying waveguide physics. Furthermore, we have developed a multi-layer version of ESM-FLOW to account for the effects of medium inhomogeneities on wave propagation. This extends the boundary-integral method to accommodate the impact of non-uniform flow on sound waves.

We have validated ESM-FLOW by comparing its results with those obtained from the FEM for sound propagation in a 3D axisymmetric flow duct. Detailed discussions of parameter selection for the model are included. The validation showed that ESM-FLOW achieves accuracy comparable to that of the FEM, with errors barely exceeding 1 dB. In contrast to the conventional boundary-integral method, the multi-layer ESM-FLOW approach overcomes the limitations imposed by uniform media. These features make ESM-FLOW highly applicable to acoustic-design applications in engines and ventilation systems.

Acknowledgements This work was supported by the National Natural Science Foundation of China (Grant No. 12304499 and Grant No. 52271343), the State Key Laboratory of Ocean Engineering (Shanghai Jiao Tong University; Grant No. GKZD010084), and the Stable Supporting Fund of National Key Laboratory of Underwater Acoustic Technology (Grant No. JCKYS2023604SSJS018). The authors would like to thank the three anonymous reviewers, whose helpful comments and suggestions have greatly improved the manuscript.

Declarations

Conflict of interest The authors declare that they have no known competing financial interests or personal relationships that could have appeared to influence the work reported in this paper.

Data availability The data are available upon reasonable request.

References

1. Kirby R, Amott K, Williams PT, Duan W (2014) On the acoustic performance of rectangular splitter silencers in the presence of mean flow. *J Sound Vib* 333(24):6295–6311
2. Chen L, Wang X, Du L, Sun X (2021) A three-dimensional analytical approach for large rectangular splitter silencers in the presence of mean flow. *J Sound Vib* 513:116404
3. Johnston G, Ogimoto K (1980) Sound radiation from a finite length unflanged circular duct with uniform axial flow. I. Theoretical analysis. *J Acoust Soc Am* 68(6):1858–1870
4. Johnston G, Ogimoto K (1980) Sound radiation from a finite length unflanged circular duct with uniform axial flow. II. Computed radiation characteristics. *J Acoust Soc Am* 68(6):1871–1883
5. Taktak M, Majdoub MA, Bentahar M, Haddar M (2012) Numerical modelling of the acoustic pressure inside an axisymmetric lined flow duct. *Arch Acoust* 37(2):151–160
6. Jha N, Das D, Tripathi A, Hota R (2019) Acoustic damping: analytical prediction with experimental validation of mixed porosity liners and analytical investigation of conical liners. *Appl Acoust* 150:179–189
7. Gupta V, Easwaran V, Munjal M (1995) A modified segmentation approach for analyzing plane wave propagation in non-uniform ducts with mean flow. *J Sound Vib* 182(5):697–707
8. Wang X, Sun X (2011) A new segmentation approach for sound propagation in non-uniform lined ducts with mean flow. *J Sound Vib* 330(10):2369–2387
9. Mercier JF, Maurel A (2016) Improved multimodal method for the acoustic propagation in waveguides with a wall impedance and a uniform flow. *Proc R Soc A Math Phys Eng Sci* 472(2190):20160094
10. Jensen FB, Kuperman WA, Porter MB, Schmidt H, Tolstoy A (2011) *Computational ocean acoustics*. Springer, New York
11. Astley RJ, Eversman W (1981) Acoustic transmission in non-uniform ducts with mean flow, part II: The finite element method. *J Sound Vib* 74(1):103–121
12. Eversman W (2003) *Turbofan noise propagation and radiation at high frequencies*. Glenn Research Center, National Aeronautics and Space Administration
13. Rao X, Zhao H, Liu Y (2023) A novel meshless method based on the virtual construction of node control domains for porous flow problems. *Eng Comput*. <https://doi.org/10.1007/s00366-022-01776-6>
14. Lin J, Bai J, Reutskiy S, Lu J (2023) A novel RBF-based meshless method for solving time-fractional transport equations in 2D and 3D arbitrary domains. *Eng Comput* 39(3):1905–1922
15. Wu T, Lee L (1994) A direct boundary integral formulation for acoustic radiation in a subsonic uniform flow. *J Sound Vib* 175(1):51–63

16. Beldi M, Barhoumi B (2015) A simple and effective axisymmetric convected Helmholtz integral equation. *Comptes Rendus Mécanique* 343(9):457–470
17. Wang F, Gu Y, Qu W, Zhang C (2020) Localized boundary knot method and its application to large-scale acoustic problems. *Comput Methods Appl Mech Eng* 361:112729
18. Wang F, Chen Z, Gong Y (2022) Local knot method for solving inverse Cauchy problems of Helmholtz equations on complicated two- and three-dimensional domains. *Int J Numer Methods Eng* 123(20):4877–4892
19. Chen Z, Wang F (2023) Localized method of fundamental solutions for acoustic analysis inside a car cavity with sound-absorbing material. *Adv Appl Math Mech* 15:182–201
20. Gregory AL, Sinayoko S, Agarwal A, Lasenby J (2015) An acoustic space-time and the Lorentz transformation in aeroacoustics. *Int J Aeroacoustics* 14(7):977–1003
21. Balin N, Casenave F, Dubois F, Duceau E, Duprey S, Terrasse I (2015) Boundary element and finite element coupling for aeroacoustics simulations. *J Comput Phys* 294:274–296
22. Mancini S, Astley RJ, Sinayoko S, Gabard G, Tournour M (2016) An integral formulation for wave propagation on weakly non-uniform potential flows. *J Sound Vib* 385:184–201
23. Juhl P (2000) Non-axisymmetric acoustic propagation in and radiation from lined ducts in a subsonic uniform mean flow: an axisymmetric boundary element formulation. *Acta Acust United Acust* 86(5):860–869
24. Barhoumi B (2017) An improved axisymmetric convected boundary element method formulation with uniform flow. *Mech Ind* 18(3):313
25. Barhoumi B, Bessrouer J (2021) A modal boundary element method for axisymmetric acoustic problems in an arbitrary uniform mean flow. *Int J Aeroacoustics* 20(1–2):35–87
26. Liu X, Wu H, Sun R, Jiang W (2022) A fast multipole boundary element method for half-space acoustic problems in a subsonic uniform flow. *Eng Anal Bound Elem* 137:16–28
27. Koopmann GH, Song L, Fahnline JB (1989) A method for computing acoustic fields based on the principle of wave superposition. *J Acoust Soc Am* 86(6):2433–2438
28. Lee S (2017) The use of equivalent source method in computational acoustics. *J Comput Acoust* 25(01):1630001
29. Johnson M, Elliott S, Baek K, Bonito GJ (1998) An equivalent source technique for calculating the sound field inside an enclosure containing scattering objects. *J Acoust Soc Am* 104(3):1221–1231
30. He T, Humphrey VF, Mo S, Fang E (2020) Three-dimensional sound scattering from transversely symmetric surface waves in deep and shallow water using the equivalent source method. *J Acoust Soc Am* 148(1):73–84
31. He T, Mo S, Guo W, Fang E (2021) Modeling propagation in shallow water with the range-dependent sea surfaces and fluid seabeds using the equivalent source method. *J Acoust Soc Am* 149(2):997–1011
32. He T, Mo S, Fang E, Wang M, Zhang R (2021) Modeling three-dimensional underwater acoustic propagation over multi-layered fluid seabeds using the equivalent source method. *J Acoust Soc Am* 150(4):2854–2864
33. He T, Wang B, Mo S, Fang E (2023) Predicting range-dependent underwater sound propagation from structural sources in shallow water using coupled finite element/equivalent source computations. *Ocean Eng* 272:113904
34. He T, Wang B, Tang S, Zhou F, Mo S, Fang E (2023) Numerical simulation of wave propagation in ice-covered ocean environments based on the equivalent-source method. *Phys Fluids* 35(4):047126
35. Parisot HD, Simon F, Piot E, Micheli F (2013) Non-intrusive planar velocity-based nearfield acoustic holography in moving fluid medium. *J Acoust Soc Am* 133(6):4087–4097
36. Bi CX, Dong BC, Zhang XZ, Zhang YB (2017) Equivalent source method-based nearfield acoustic holography in a moving medium. *J Vib Acoust* 139(5):051017
37. Wang ZH, Bi CX, Zhang XZ, Zhang YB (2017) Sound field prediction and separation in a moving medium using the time-domain equivalent source method. *Acta Acust United Acust* 103(3):401–410
38. Bi CX, Li YC, Zhang YB, Zhang XZ, Xu L (2019) Signal reconstruction of moving sound sources with a fixed microphone array. *Mech Syst Signal Process* 118:277–289
39. Waldvogel J (2006) Fast construction of the Fejér and Clenshaw–Curtis quadrature rules. *BIT Numer Math* 46(1):195–202
40. Zhang P, Wu T, Lee L (1996) A coupled FEM/BEM formulation for acoustic radiation in a subsonic non-uniform flow. *J Sound Vib* 192(1):333–347
41. Myers M (1980) On the acoustic boundary condition in the presence of flow. *J Sound Vib* 71(3):429–434
42. Wright L, Robinson SP, Humphrey VF (2009) Prediction of acoustic radiation from axisymmetric surfaces with arbitrary boundary conditions using the boundary element method on a distributed computing system. *J Acoust Soc Am* 125(3):1374–1383
43. Sheng X, Peng Y, Xiao X (2019) Boundary integral equations for sound radiation from a harmonically vibrating body moving uniformly in a free space. *J Acoust Soc Am* 146(6):4493–4506
44. Tsinopoulos SV, Agnantiaris JP, Polyzos D (1999) An advanced boundary element/fast Fourier transform axisymmetric formulation for acoustic radiation and wave scattering problems. *J Acoust Soc Am* 105(3):1517–1526
45. Xiang Y, Lu J, Huang Y (2012) A fast wave superposition spectral method with complex radius vector combined with two-dimensional fast Fourier transform algorithm for acoustic radiation of axisymmetric bodies. *J Sound Vib* 331(6):1441–1454
46. Zhang P, Wu T (1997) A hypersingular integral formulation for acoustic radiation in moving flows. *J Sound Vib* 206(3):309–326
47. Duff IS, Koster J (2001) On algorithms for permuting large entries to the diagonal of a sparse matrix. *SIAM J Matrix Anal Appl* 22(4):973–996

Publisher's Note Springer Nature remains neutral with regard to jurisdictional claims in published maps and institutional affiliations.

Springer Nature or its licensor (e.g. a society or other partner) holds exclusive rights to this article under a publishing agreement with the author(s) or other rightsholder(s); author self-archiving of the accepted manuscript version of this article is solely governed by the terms of such publishing agreement and applicable law.

Authors and Affiliations

Tengjiao He^{1,5}  · Shiqi Mo² · Erzheng Fang² · Xinyu Liu³ · Yong Li⁴ 

✉ Yong Li
yongli@tongji.edu.cn
Tengjiao He
hetengjiao@sjtu.edu.cn
Shiqi Mo
moshiqi@hrbeu.edu.cn
Erzheng Fang
fangerzheng@hotmail.com
Xinyu Liu
liuxinyu@cssrc.com.cn

² College of Underwater Acoustic Engineering,
Harbin Engineering University, Harbin 150001,
People's Republic of China

³ China Ship Scientific Research Center, Wuxi 214082,
People's Republic of China

⁴ Institute of Acoustics, School of Physics Science
and Engineering, Tongji University, Shanghai 200092,
People's Republic of China

⁵ School of Naval Architecture, Ocean & Civil Engineering,
Shanghai Jiao Tong University, Shanghai 200240,
People's Republic of China

¹ Key Laboratory of Marine Intelligent Equipment
and System, Ministry of Education, Shanghai Jiao Tong
University, Shanghai 200240, People's Republic of China